Potential fatigue strength improvement of AA 5083-H111 notched parts by wire brush hammering: Experimental analysis and numerical simulation

Naziha Sidhom [a], Naoufel Ben Moussa [a], Sameh Janeb [a], Chedly Braham [b], Habib Sidhom [a,*]

[a] Mechanical, Material and Processes Laboratory (LR99ES05), ESSTT, 5, Avenue Taha Hussein 1008, University of Tunis, Tunis, Tunisia
[b] Laboratoire de Procédés et Ingénierie en Mécanique et Matériaux (PIMM-UMR CNRS 8006), ENSAM, 151, Boulevard de l'Hôpital, 75013 Paris, France

ABSTRACT

The effects of milling as machining process and a post-machining treatment by wire-brush hammering, on the near surface layer characteristics of AA 5083-H111 were investigated. Surface texture, work-hardening and residual stress profiles were determined by roughness measurement, scanning electron microscope (SEM) examinations, microhardness and X-ray diffraction (XRD) measurements. The effects of surface preparation on the fatigue strength were assessed by bending fatigue tests performed on notched samples for two loading stress ratios $R_{0.1}$ and $R_{0.5}$. It is found that the bending fatigue limit at $R_{0.1}$ and 10^7 cycles is 20% increased, with respect to the machined surface, by wire-brush hammering. This improvement was discussed on the basis of the role of surface topography, stabilized residual stress and work-hardening on the fatigue-crack network nucleation and growth. The effects biaxial residual stress field and surface work-hardening were taken into account in the finite element model. A multi-axial fatigue criterion was proposed to predict the fatigue strength of aluminum alloy notched parts for both machined and treated states.

1. Introduction

Manufactured components and assembled structures used in automotive, railway, vessel and aerospace industries are regularly subjected to cyclic loading and they are consequently prone to fatigue damage. The damage consists of fatigue-crack network nucleation and growth leading to fracture. In almost all cases of machined components, fatigue-cracks initiate at the surface due to micro stress concentrations caused by machining marks, grooves and exposed inclusions. That is why the conditioning of the surface to resist a crack initiation and earlier crack growth by mechanical surface treatments is required for many advanced applications involving high-cyclic loading. The surface conditioning, depending upon material and applications, includes simple as well as double treatments:

– Simple treatments such as conventional shot peening (CSP) [1–6], hammer peening (HP) [7,8] low plasticity burnishing (LPB) [9], deep-rolling (DR) [10], laser peening (LP) [11,12], ultrasonic peening [13] and pulsed electron beam treatments [14] were performed for steels, aluminum alloys and titanium alloys.

– Double treatments such as double peening [15], nitriding and shot peening [16], plasma-carburizing and deep-rolling [17], laser-assisted burnishing [18] and ultrasound-aided deep rolling [19], were usually used for enhancing fatigue strength by combining the beneficial effect of each treatment.

All these treatments induce typical surface topography, compressive residual stress, work-hardening and microstructure changes at the near-surface regions. However, some of these changes have opposite effects on the fatigue-crack nucleation and growth. Indeed, it is reported that surface roughness accelerates crack nucleation without effect on crack propagation [20,21]. In contrast work-hardening retards nucleation and accelerates crack propagation [22–24], while compressive residual stresses are beneficial for both fatigue-crack nucleation and growth strength [20,25,26]. Therefore, a large number of studies [5,6] have been carried out and reported significant information on the optimization of well-known mechanical surface treatments processes in order to improve their surface effects balance. Other study was devoted to the development of new and more efficient methods for fatigue performance enhancement [11].

Concerning the process optimization, it has been reported that the close monitoring of parameters such as media, intensity and coverage of peening process optimize the surface characteristics that can effectively increase fatigue-crack initiation life time such

* Corresponding author. Tel.: +216 71 496 066; fax: +216 71 391 166.
  E-mail addresses: habib.sidhom@gmail.com, Habib.sidhom@esstt.rnu.tn
(H. Sidhom).

Nomenclature

$R_{0.1}$, $R_{0.5}$	loading ratio for stress controlled tests
K_t	stress concentration factor
σ_n	nominal stress (MPa)
F_{max}	maximum applied force in stress controlled tests (N)
a	distance between the applied force points (mm)
b	distance between roller axis (mm)
L	bending specimen width (mm)
x	notch depth in bending specimen (mm)
e	bending specimen thickness (mm)
Ra	arithmetical mean roughness (μm)
Rt	maximum height of the roughness profile (μm)
σ_D^{max}	high cycle fatigue limit at 10^7 cycles (MPa)
σ_{eq}	equivalent stress appearing in the sines criterion (MPa)
J_2	second invariant of the stress deviator tensor (MPa^2)
$\sqrt{J_{2,a}}$	square root of the amplitude of J$_2$ (MPa)
P_m	mean hydrostatic pressure (MPa)
α, β	material parameters appearing in the sines criterion
$\underline{\underline{\sigma}}(t)$	cyclic stress tensor at an instant t
$\underline{\underline{S}}(t_i)$, $\underline{\underline{S}}(t_j)$	cyclic stress deviator tensor at two different instants t_i and t_j, respectively
k	initial yield stress in tension (MPa)
E	Young modulus (GPa)
v	Poisson ratio
$\dot{p}$	cumulated plastic strain rate (S^{-1})
X	variable of the nonlinear kinematic hardening law
C, γ	material constants of the nonlinear kinematic hardening law
R, Q	material constants of the isotropic hardening law
σ_{11}^R, σ_2^R	residual stresses in loading and transverse directions, respectively (MPa)
f	feed velocity (mm/min)
Vc	cutting speed (m/s)
ap	depth of cut (mm)
D	brush diameter (mm)
d	wire diameter (mm)
l	wire length (mm)
Vs	brush rotational speed (rpm)
V_f	work speed (mm/min)
P	percentage of effective wire compression (%)
N_{passes}	number of passes (passes)
λ	wave length of the X-ray (nm)
θ	Bragg angle (°)
ψ	Tilt angle: angle between the normal of the sample and the normal of the diffracting plane (°)
ϕ	angle between a fixed direction in the plane of the sample and the projection in that plane of the normal of the diffracting plane (°)
H_V	Vickers hardness

as compressive residual stress and work-hardening. In addition, the controlled shot peening (CSP) process minimizes the detrimental effect of surface roughness and defects. Therefore, the shot peening of aluminum alloys is usually performed with lighter media such as glass or ceramic beads with low intensity of peening in order to achieve the satisfactory compromise between beneficial compressive residual stresses and detrimental effects on surface quality. Steel shots increase surface roughness and cause the surface ferrous contaminations that induce undesired galvanic effects [27]. Luo et al. [28] reported that the steel shot peened surface of AA 7075-T6 exhibits a limited beneficial effect on the fatigue behavior at only a net 7% increase in fatigue life. On the other hand, peening with light media such as glass or ceramic beads improves significantly the fatigue resistance.

Concerning the development of new surface enhancement technology, it is reported that processes such as low plasticity burnishing, laser peening, ultrasonic peening and/or pulsed electron beam treatments provide compression in the surface layer of sufficient depth and effectively eliminate the surface degradation. Then, they offer the opportunity to significant improvements in fatigue performance on large variety of materials. Nevertheless, the successful fatigue enhancement from these methods can be compromised by some technical difficulties, induced surface integrity changes [13,14,18] and high cost in comparison with the widely used conventional shot peening in spite of its detrimental effects on surface quality [22,28]. Therefore, the exploration of alternative techniques as a potential replacement for shot peening must resolve the controversial effects exerted by this treatment on the surface layers, with a comparable beneficial compressive residual stresses and work-hardening at low cost.

Wire-brush hammering is a more recent method for introducing a compressive residual stress in the surface layer without a large effect on surface roughness. The efficiency of this process is now well established, for die steels [29] and austenitic stainless steels [30] in dry [31], as well as in cryogenic [32], environment. Therefore, its extension to components made of aluminum alloys could generate much interest for aerospace and shipbuilding

industries. This paper explore, the potentialities of wire-brush hammering to enhance the fatigue performance of AA 5083-H111 by cold work-hardening method as an alternative to shot peening. This aluminum is frequently used in the fatigue-critical shipbuilding components owing to its small specific weight, high corrosion resistance to various aggressive environments and has relatively good mechanical properties. The wire-brush hammering conditions were selected by comparing their effects with shot peening effects on surface roughness, work-hardening and compressive residual stress field. The potentialities of fatigue improvement were assessed by comparing the fatigue limit at 10^7 cycles of wire-brushed hammered surfaces with that of machined surface. Fatigue limits were determined by four point bending fatigue tests performed on notched specimens for two loading ratios, $R_{0.1}$ and $R_{0.5}$. The residual stress and work-hardening profiles were experimentally investigated before and after fatigue loading in order to establish their effect on crack initiation sites and consequences on fatigue life improvement. Numerical procedure is used to take into account the biaxial residual stress field and surface work-hardening in order to identify the Sines criterion parameters. This multi-axial fatigue criterion was validated as a predictive tool of AA5083-H111 fatigue-crack nucleation.

2. Material

The experiment is performed on the aluminum–magnesium alloy AA5083 (AlMg4.5) supplied in the form of 10 mm thick rolled plate. The chemical composition of this alloy is given in Table 1. The material received in the H111 thermo-mechanical treatment, consisting of a cold work-hardening following a solution heat treatment for 2 h at 623 K. The resulting microstructure, shown in Fig. 1, consists of slightly elongated grains on the rolling plane (Fig. 1a) and equiaxial grains on the cross-section through the plate thickness (Fig. 1b). The grain size varies from 50 μm to 150 μm.

The mechanical properties of the material along the rolling direction were acquired by means of monotonic tensile tests using normalized plane hourglass specimens. The results, summarized in

Table 1
Chemical composition of AA 5083-H111 (% weight).

Si	Fe	Cu	Mn	Mg	Cr	Ni	Zn	Ti	Pb	Al
0.15	0.28	0.02	0.761	4.24	0.133	0.002	0.01	0.014	0.0001	Bal
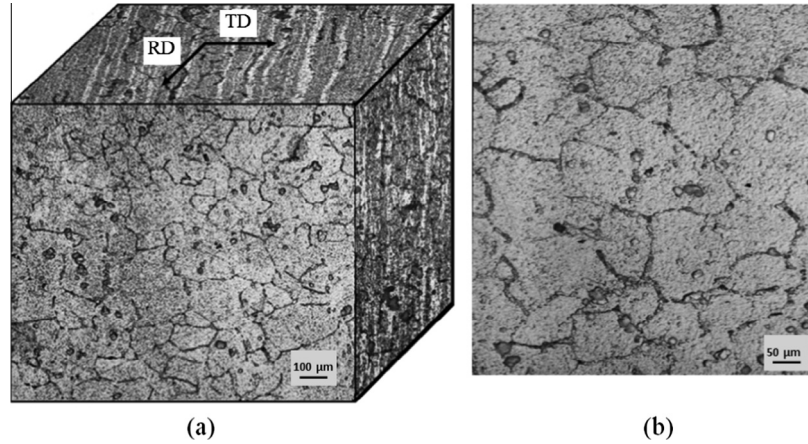
Fig. 1. Microstructure of AA 5083-H111, (a) rolled plate, and (b) microstructure.

Table 2
Mechanical properties of AA 5083 H111.

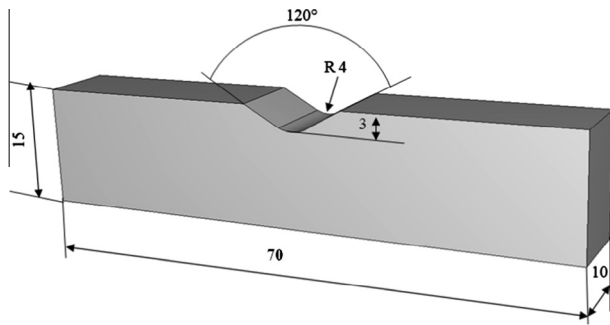| Rp$_{0.2}$ (MPa)	Rm (MPa)	A (%)	E (GPa)	Hv$_{0.1}$
140	312	24	72	82

Fig. 2. Notched fatigue specimen.

Table 2, show a yield stress less than 140 MPa, combined with good alloy ductility (total elongation of 24%). The bulk material hardness is measured about 80 Hv.

3. Surface preparation modes

Prismatic fatigue samples, with circular profile notch geometry defined by radius and depth as shown in Fig. 2, were manufactured by milling and post-machined by wire-brush hammering:

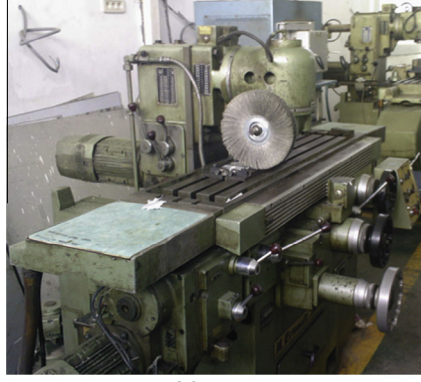### 3.1. Machining by milling

Sample notches were machined by numerical controlled machine using high-speed steel tools with an end mill diameter of 8 mm. The cutting conditions for the milling process are reported in Table 3.

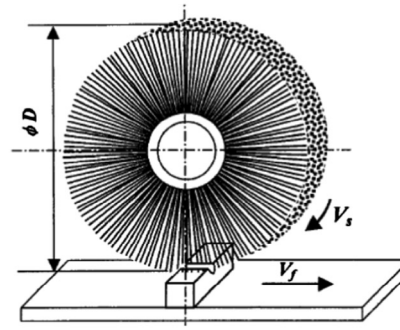### 3.2. Post-machining by wire-brush hammering

Wire-brush hammering was applied to the fatigue samples, previously machined by milling, using stainless steel wire-brush. The experimental setup used for wire-brushing experiments is shown in Fig. 3a. The brush used in this study is illustrated in Fig. 3b and its characteristics are given in Table 4. This brush was set on a conventional milling machine as shown in Fig. 3a. During the wire-brushing process, the wires were effectively compressed by 3% of their length (i.e., the surface of the notch was set at 2.4 mm from the inner end of the wires) to ensure efficient hammering without removal material. The experimental conditions of the wire-brush hammering are listed in Table 4.

4. Experimental procedure

Morphology of machined and wire-brush hammered surfaces were characterized by scanning electron microscope (SEM) examinations and roughness measurements using a Stylus-type profilometer. Work-hardening, induced by the processes was characterized by microhardness measurements using a microhardness tester set type Shimadzu at a load of 50 gf. The near surface residual stress distributions were evaluated before and after loading using the X-ray diffraction method (XRD) performed on the Proto XRD device,

Table 3
Machining conditions of fatigue specimen notch root.

Feed f (mm/rev)	Cutting speed Vc (m/s)	Depth of cut ap (mm)		Lubrication mode
		Roughing	Finishing	
0.2	23	2.5	0.5	Without lubrication

Fig. 3. Wire brush hammering apparatus, (a) experimental setup, and (b) schematic form of wire brush hammering.

Table 4
Wire brush hammering conditions.

Wire material	Stainless steel
Brush diameter	D = 230 mm
Wire diameter	d = 0.1 mm
Wire length	l = 80 mm
Brush rotational speed	Vs = 630 rpm
Work speed	V_f = 12, 32 and 50 mm/min
Percentage of effective wire compression	P = 3%
Number of passes	N_{passes} = 7

Table 5
X-ray diffraction parameters.

Radiation	Cr Kα radiation (λ = 0.229 nm)
Voltage	20 kV
Current	5 mA
X-ray diffraction planes	{3 1 1}, 2θ = 139.5
Beam diameter	2 mm
Angles ϕ	0° and 90° (2 directions)
ψ Oscillation	±3°
Tilt angles ψ	17 angles from −37.27°

according to the conditions listed in Table 5. For in-depth measurements, material removal was performed by electro polishing with an electrolyte composed by 8% (by volume) perchloric acid solution mixed in solution with 92% (by volume) of glacial acetic acid.

The fatigue improvement by wire-brush hammering was assessed by four-point bending fatigue tests on notched machined and hammered specimens using an MTS-810 servo-hydraulic testing system, in order to determine the fatigue limit at 10^7 cycles. Fatigue experiments were conducted according to stair case method [33]for two stress ratios $R_{0.1}$ and $R_{0.5}$. Fatigue tests were stopped beyond 10^7 cycles if no fracture occurred. Tests were carried out at frequency equal to 30 Hz, using a notched fatigue-bending specimen with a stress concentration factor of K_t = 1.6 in order to assess the efficiency of the wire-brush hammering as post-machining treatment of an industrial component with varying geometries (Fig. 4). In addition, the selected geometry offers a biaxial loading at the notch root making the investigation of fatigue-crack nucleation mechanisms easier and multi-axial fatigue criteria applications meaningful. The application of four-point bending fatigue tests on the notched specimens requires the determination of the forces to be applied for each nominal stress level, according to Eq. (1) deduced from loading geometry shown in Fig. 4.

$$\sigma_n = \frac{3F(a-b)(L-2x)}{2e(L)^3} \qquad (1)$$

where F is the applied force required to stress controlled tests, e is the specimen thickness which is taken as 10 mm, x is the notch depth which is 3 mm, L is the specimen width which is 15 mm, a is the distance between the applied force points which is 60 mm and b is the distance between axis, which is taken as 30 mm.

The role of the surface characteristics on the fatigue-crack nucleation and growth was investigated by SEM examinations of notch root surface of fatigue-loaded specimens and fracture surface of broken fatigue specimens.

5. Experimental results

5.1. Optimization of the wire-brush hammering conditions

The optimal wire-brush hammering conditions were selected based on the surface characteristics controlling fatigue-crack nucleation and growth resistance like the surface roughness, near surface residual stress and surface hardness. Previous studies [30,34,35] reported that for the imposed brush characteristics, the brush rotational speed (Vs), wire-brush feed (V_f), and number of passes (N_{passes}) could have a crucial influence on surface characteristics. However, in this investigation, as the same brush was used for all the experiments, the optimized parameter considered was only the wire-brush feed (V_f) which was varied from 12 to 50 mm/min. These conditions were applied to the notched part of the fatigue specimens and Almen "N" type strips. The arc height is measured, on standard test strips made of spring steel, for investigated wire-brush hammering and shot peening conditions. After that, the treated surfaces were investigated and the measured characteristics were reported with the corresponding value of Almen intensity in Table 6. The result analysis leads to the conclusion that the post machining by wire-brush hammering can be controlled, like shot peening process, by Almen "N" type strips - which are used usually for glass bead peen and ceramic bead peen. Therefore, Almen intensity increases with the wire-brush feed (V_f) and the duration of shot peening. On the other hand, it is clear that the greater is the Almen intensity, the greater are compressive residual stress and hardness levels. On the basis of criteria related to high compressive residual stress, high work-hardening and low surface roughness, the condition corresponding to set B3 (V_f = 50 mm/min, Table 6) is selected for wire-brush hammering of the AA5083-H111 fatigue test specimens in order to assess the fatigue improvement capacities of this recent cold working treatment. This condition is considered, on the basis of Almen intensity, equivalent to that of shot peening (SP1) as given in Table 6. In addition, the induced work-hardening and compressive residual stress characteristics are very similar without the drawback of roughness.
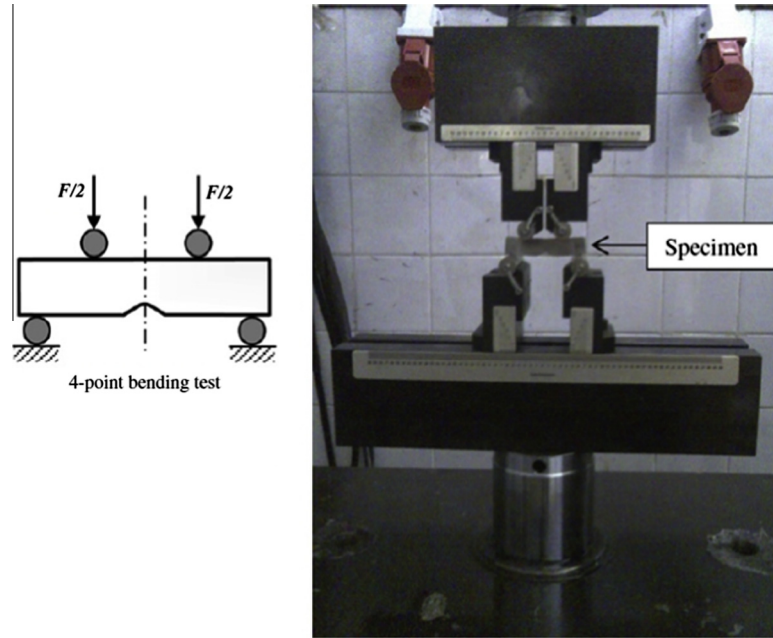
Fig. 4. Device of 4-point plane-bending fatigue test.

Table 6
Effect of wire brush hammering and shot peening conditions on the surface characteristics.

Surface preparation mode	Treatment conditions						Surface roughness		Surface hardness Hv$_{0.05}$	Residual stress (MPa)	
	Vs (rpm)	N$_{passes}$ (passes)	P (%)	V$_f$ (mm/min)	Time (min)	Almen intensity	Ra (μm)	Rt (μm)		σ_{11}^R (MPa)	σ_{22}^R (MPa)
Brushed B1	630	7	3	12		F0.6N	3	24.3		−135 ± 20	−65 ± 20
Brushed B2	630	7	3	32		F3.2N	3.4	21.6		−140 ± 10	−130 ± 20
Brushed B3	630	7	3	50		F5.9N	1.8	12.5	144	−180 ± 20	−125 ± 35
Shot peened SP1		–			8	F6.7N	9	56.6	146	−188 ± 16	−148 ± 8
Shot peened SP2					12	F7.1N	9.7	58.5		−211 ± 10	−161 ± 10
Shot peened SP3					20	F8.1N	9.2	66.2		−206 ± 14	−136 ± 12

Table 7
Characteristics of machined and wire brush hammered AA5083-H111 surfaces before fatigue loading.

Surface preparation mode	A Roughness		B Initial work hardening (Hv$_{0.05}$)			C Initial residual stress				D Surface morphology
	Ra (μm)	Rt (μm)	Near surface hardness	Work hardening depth (μm)	Bulk material Hardness	σ_{11}^R (MPa)	Depth (μm)	σ_{22}^R (MPa)	Depth (μm)	
Machining	2.4	20.5	110 ± 3	300	80 ± 3	−40 ± 11	20	−22 ± 8	40	Machining grooves (Fig. 5a)
Wire brush hammering	1.8	12.5	144 ± 5	300		−180 ± 20	80	−125 ± 35	50	Hammered aspect (Fig. 5b)

The quality of the prepared surfaces was evaluated qualitatively by SEM examination and quantitatively by roughness, micro-hardness and residual stress measurements. The wire-brush hammering surface characteristics was compared with those of machined surface in Table 7.

5.1.1. Surface morphology and roughness

SEM observations reveal grooves on milled surface (Fig. 5a) and show that subsequent brush hammering removes completely these machining grooves and leads to a hammered morphology similar to shot-peened surfaces (Fig. 5b). Therefore, the plastic deformation induced by successive passes of the wire-brush hammering leads to fewer high irregularities of surface with less sharpness than the roughness profiles of the machined surfaces (Fig. 6).

This explains the reduction of roughness values Ra and Rt with respect to machined surface as indicated in Column A of Table 7. In terms of roughness, wire-brush hammering, when performed in the optimal condition (B3 condition), improves surface micro geometrical quality by a significant decreasing of Rt from 20.5 μm in the machined condition to 12.5 μm in the brushed condition. The same tendency was observed for the mean roughness Ra that is slightly reduced from 2.4 μm for machined surface to 1.8 μm for the wire-brush hammered one.

5.1.2. Work-hardening

Work-hardening induced by machining and wire-brush hammering processes was investigated by cross-section micro-hardness measurements (Hv$_{0.05}$). Three measurements were
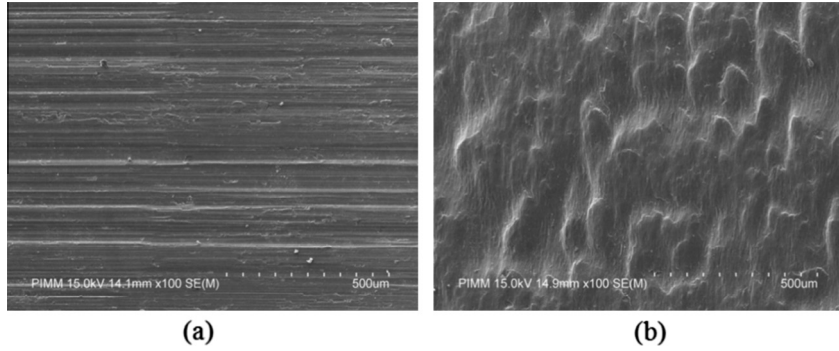
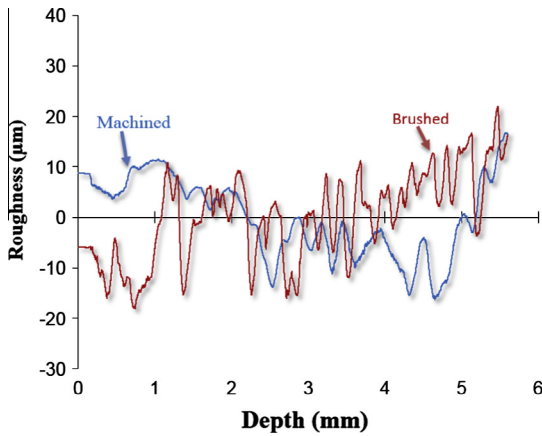**Fig. 5.** Surface morphology, (a) machined, and (b) wire brush hammered.

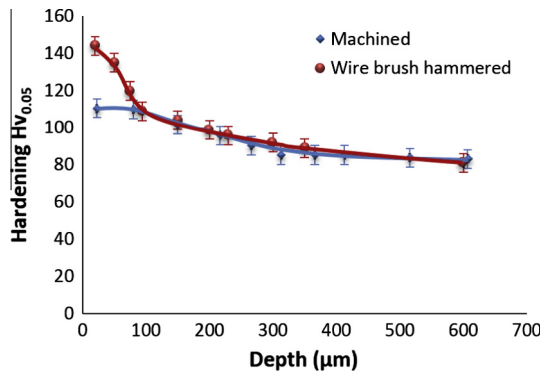**Fig. 6.** Roughness profiles of AA5083-H111 machined and wire brush hammered.

Fig. 7. Effect of machining and wire brush hammering on the work hardening characteristics of AA 5083-H111.

performed at each depth and averaged in order to account for measurement errors. The resulting micro-hardness profiles are compared in Fig. 7. It appears clearly that wire-brush hammering of AA5083-H111 machined surface induces an additional near surface work-hardening. The work-hardening profile characteristics such as surface hardness (at 20 μm from the surface) and hardened layers depth are indicated in Column B of Table 7. A hardness of 144 Hv$_{0.05}$ is measured at 20 μm from the surface of the wire-brush hammered material whereas only a value of 110 Hv is measured at the same thickness for the machined material. Therefore, the rate of the hardening of the surface with respect to the bulk material (80 Hv to 83 Hv) is increased by 75% for the wire-brush hammered and only by 35% for the milled surfaces. In addition, the extent of the additional work-hardening induced by wire-brush hammering is limited to 100 μm from the surface compared to the depth of machined induced work-hardening (300 μm).

These observations lead to the conclusion that the successive hammering by the wire-brush causes an intense superficial plastic strain of near surface layers.

5.1.3. Residual stresses

Machining and wire-brush hammering operations induce residual stresses in the processed affected layers. For the wire-brush hammering, the residual stresses are produced by the transfer of kinetic energy from a moving mass of wire into the surface of material with the capacity to plastically deform. The wire-brush bombarding of the surface leading to plastic deformation of thin surface layers which changes the dislocation density. The elastically stressed sub-surface layers try to return in their initial state after treatment, but this is prevented by the permanent plastic deformed surface layers. Then a compressive residual stress field is generated on the surface and in the near surface layers, while tensile residual stresses are developed in the underneath layers. The biaxial distribution of residual stresses generated by both machining and wire-brush hammering was investigated by XRD measurements. Several measurements were carried out in the notch root of the fatigue samples in order to verify the homogeneity of the treatment. The initial stress profiles in the two orthogonal directions (before fatigue testing) are illustrated in Fig. 8a and b, for machined surface and wire-brush hammering surface respectively. Surface residual stress levels are reported in Table 7 (Column C). The analysis of the residual stress field induced by machining reveals a very thin near surface layer (20–40 μm) affected by low compressive residual stresses (−20 MPa to −40 MPa) balanced by an equivalent sub-surface tensile residual stresses (Fig. 8a). This suggests that the selected milling finishing conditions are appropriate as confirmed by low induced cold work-hardening showed in Fig. 7. However, the surface subjected to wire-brush hammering after milling is characterized by both high and deep compressive residual stress profiles (Fig. 8b). In addition, the high levels of the stresses are achieved at surface for the two measurement directions. They reached about 180 MPa (equivalent to 1.28 bulk material yield stress) in the longitudinal direction and −125 MPa (equivalent to 0.9 bulk material yield stress) in the transversal direction. The wire-brush compressed layers reached value ranging from 50 to 80 μm. These layers are considered very thin compared the layers affected by shot peening usually ranging from 200 to 800 μm.

5.2. Fatigue limit evaluation

The analysis of bending fatigue test data, performed in accordance to stair case method, provides the high cycle fatigue limits at 10^7 cycles expressed by notch root nominal stress $\sigma_D^{\max}$ (10^7 cycles). The values of $\sigma_D^{\max}$ (10^7 cycles), for the machined and wire-brush hammered surfaces are compared in Table 8. The S–N curves, showed in Fig. 9, compare the effect of cold-work treatment
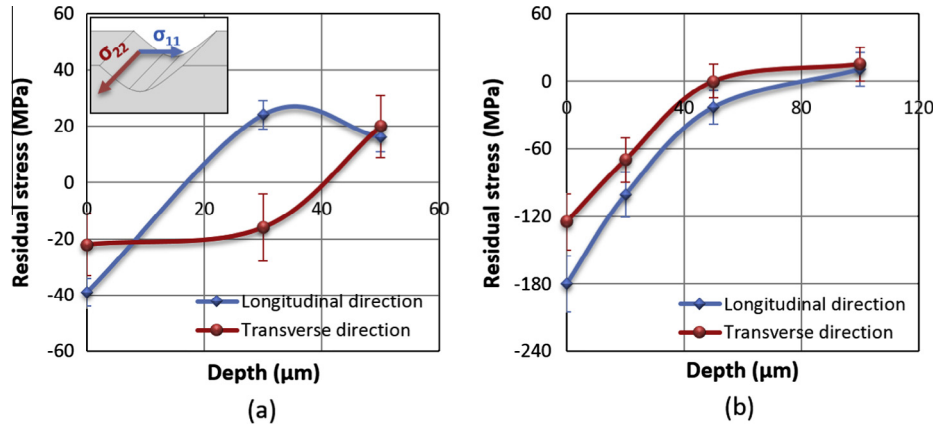
Fig. 8. Initial residual stress profiles (loading direction σ_{11} and transverse direction σ_{22}), (a) machining induced residual stress, and (b) Wire brush hammering induced residual stress.

Table 8
Effect of stabilized surface characteristics and stress ratio on fatigue limit of AA 5083-H111.

Surface preparation mode	Surface characteristics						Fatigue results		
	Surface roughness		Stabilized work hardening		Surface stabilized residual Stress				
	Ra (μm)	Rt (μm)	Surface hardness $Hv_{0.05}$	Hardening depth e (μm)	σ_{11}^{RS} (MPa)	σ_{22}^{RS} (MPa)	Stress ratio R	Fatigue limit[*] at 10^7 cycles $\sigma_{D\ (MPa)}$	Fatigue improvement rate%
Machined	2.4	20.5	134 ± 5 –	1200	−120 ± 11 –	−40 ± 6 0.5	0.1 89	57	
Wire brush hammered	1.8	12.5	140 ± 6 −170 ± 20	800	−119 ± 20 −107 ± 22	−62 ± 9 0.5	0.1 94	68.5 5	20

[*] Maximum nominal stress at notch root.

by wire-brush hammering on the low cycle fatigue (LCF) as well as on the high cycle fatigue (HCF) behavior of AA5083-H111. It is clearly observed from Fig. 9 that the fatigue limits of the wire-brush hammered specimens were significantly higher than those of the machined specimens for $N > 10^6$ cycles. An improvement rate of HCF strength of about 20% for a load ratio $R_{0.1}$ and only 5% for a load ratio $R_{0.5}$ is recorded when machined surface of AA5083-H111 is wire-brush hammered. This improvement is related to the effect of the stabilized surface characteristics on the fatigue-crack nucleation and growth resistance.

5.3. Evaluation of stabilized surface characteristics

The initial profiles of cold work-hardening and near surface residual stress field induced by both machining and wire-brush hammering, undergo some changes under cyclic loading. The evolution is expected when the residual stresses combine with the applied stresses exceed the yield limit of material. This condition is firstly reached for some applied stress range at the notch root zone of fatigue specimen causing local monotonic (first cycle) and cyclic (further cycles) plastic deformation. Then the plastic misfit between hardened layers and bulk material could be modified and consequently the work-hardening and residual stress fields were modified simultaneously. In order to verify the occurrence of this phenomenon and its impact on the fatigue behavior, we investigate the microhardness and residual stress profiles of machined and wire-brush hammered samples cycled up to 10^7 cycles at an imposed stress level corresponding to their respective fatigue limits.

5.3.1. Stabilized work-hardening

The post fatigue micro-hardness profile, compared to the unloaded one, proves that the surface layers (less than 50 μm from the surface) of machined notch root zone are deformed at an imposed cyclic applied stress very close to fatigue limit (Fig. 10a). However, the sub-layers fatigue induced work-hardening is less significant but more extended (until 1300 μm beneath the surface) with respect to unloaded specimen. In contrast, there is no change in wire-brush hammered microhardness profile, up to 100 μm from the surface, after fatigue loading at an imposed applied stress corresponding to fatigue limits at 10^7 cycles (Fig. 10b). However under layers, up to 800 μm, of notch root zone were significantly hardened. The modification of the work-hardening, by fatigue loading, promotes a new residual stress distribution.

5.3.2. Stabilized residual stresses

The XRD measurements of the post fatigue residual stress were performed at the notch root zone of fatigue tested specimen for the stress level close to the fatigue limit. The profiles before and after loading, compared in Figs. 11 and 12, indicated that the applying bending fatigue stress modifies the magnitude and depth of residual stresses induced by both machining and wire-brush hammering. Indeed, fatigue loading generates, in the loading direction of machined sample, a higher (−100 MPa after cyclic loading instead of −40 MPa before loading) and deeper (more than 120 μm after cyclic loading instead of 20 μm before loading) compressive residual stress (Fig. 11a). However, there is no change of residual stress distribution in the transverse direction (Fig. 11b). This result is in good agreement with work-hardening modification related to plastic misfit change under fatigue loading observed in Fig. 10a. On the other hand, the post fatigue residual stress profiles of wire-brush hammered samples, show various degree of the near surface residual stress relaxation (Fig. 12). In outermost surface, the compressive residual stress relaxed by 72% of its initial value in the loading direction (Fig. 12a) and by 48% of its initial value in the transverse direction (Fig. 12b). In sub-layer, both the depth and magnitude of the compressive residual stresses increase with respect to the initial profile. Then the initial tensile residual stress under layers overcome compressive up to depth greater than 150 μm.
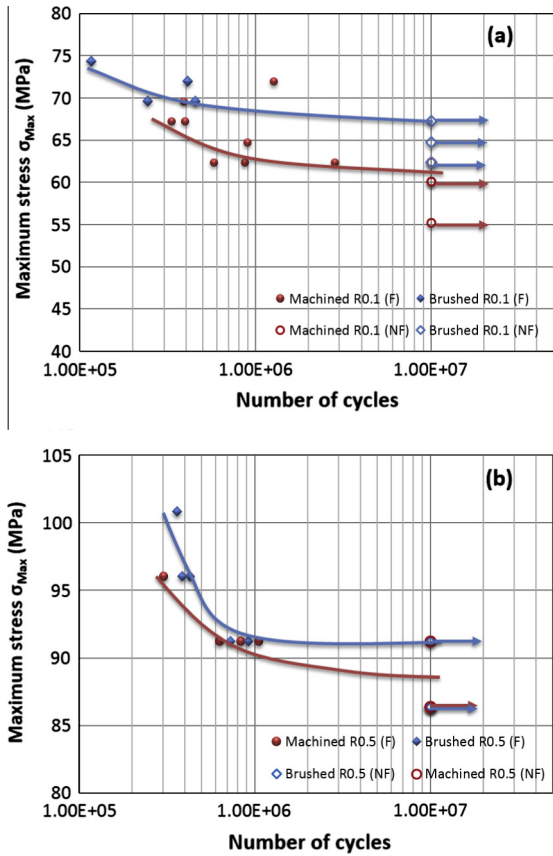
Fig. 9. Improvement of fatigue limit by wire brush hammering (S–N curves, (a) stress ratio = $R_{0.1}$, and (b) stress ratio = R0.5).

5.4. Fatigue crack nucleation and growth

The fatigue-crack nucleation and growth were investigated by SEM examinations of ruptured and unruptured fatigue tested specimens in order to identify the role of the surface characteristics on the fatigue-crack network characteristics and their stability. The crack network configuration was qualitatively investigated by SEM examination of the tested specimen surface at the notch root zone. However, the crack nucleation points and local fatigue-crack growth rate were identified by SEM micro-fractographic analysis.

5.4.1. Fatigue crack nucleation

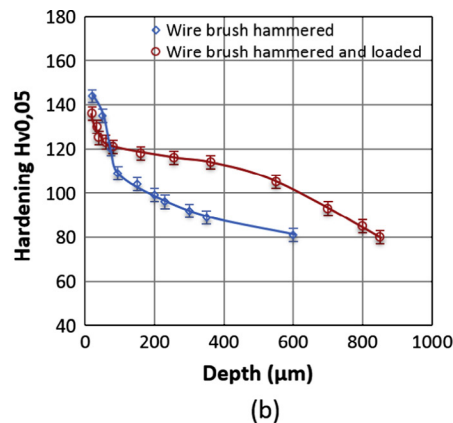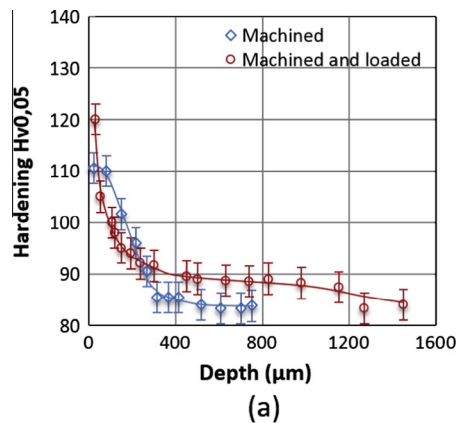The notch root surface examination of fatigue fractured specimens shows randomly distributed short cracks with an average length less than 200 μm, emerging at the wire-brush hammered surface. These cracks are mostly associated with the topographical features generated by the hammering of the surface by the steel wires of the brush (Fig. 13a). This configuration, of separate micro-cracks associated with the compressive residual stress field, confers a great stability of the fatigue-crack network with respect to the coalescence. However, the machined surface SEM examinations reveal a single long crack oriented perpendicular to loading direction that likely propagates until total fracture (Fig. 13b). On the other hand, the SEM observations of the fracture surfaces reveal several crack sources. Mostly of these cracks are located close to the surface at 20–50 μm for the machined samples (Fig. 14a) and beneath the surface at 70–150 μm for the wire-brush hammered samples (Fig. 14b). The subsurface fatigue-crack initiation is likely attributed to position of high peak stress resulting from summation of applied loading stress and stabilized residual stress.

5.4.2. Fatigue crack growth

The fatigue-crack propagation in AA 5083-H111 occurs with a ductile manner for both machined and wire-brush hammered surfaces. It is particularly characterized by the formation of serrated fatigue striation more evidenced beneath the hardened layers (Fig. 15). The quantitative analysis of the micro-fractographs leads to the assessment of the local (at the grain scale) fatigue-crack propagation rate. This rate varies from 0.5 μm/cycle-at 300 μm (Fig. 15a) from the surface to 1 μm/cycle at 500 μm (Fig. 15b) from the surface of wire-brush hammered specimen loaded at stress level close to fatigue limit. At the overload zone, corresponding to final fracture, dimples resulting from the well-known ductile fracture mode of the AA5083-H111 were observed (Fig. 16).

6. Numerical simulation and multi-axial criterion

Sines multi-axial criterion was used to take advantage of the experimental results for calculating HCF strength of machined and wire-brush hammered in AA5083 [36]. This criterion was employed because it is more realistic for ductile materials and frequently used in engineering structure calculation. A numerical procedure was developed in order to take into account the initial biaxial residual stress field and its evolution under cyclic loading. The numerical procedure was accounted for the effect of work-hardening on the fatigue behavior using Sines multi-axial criterion. Whereas, the effect of surface roughness was neglected according to Novovic [21] who suggested that when surface roughness is 2.5–5 μm Ra, surface residual stress is often a better indicator of fatigue performance than surface topography.

Fig. 10. Work hardening evolution under cyclic loading at 10^7 cycles, (a) machined and loaded at σ_{max} = 57.6 MPa and $R_{0.1}$, and (b) wire brush hammered and loaded at σ_{max} = 69.6 MPa and $R_{0.1}$.
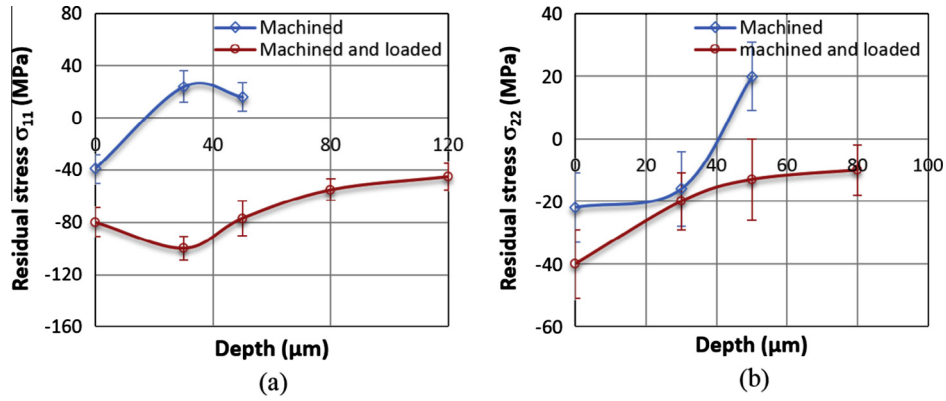
Fig. 11. Machining residual stress evolution under cyclic loading at $\sigma_{max} = 57.6$ MPa and $R_{0.1}$, (a) loading direction, and (b) transverse direction.
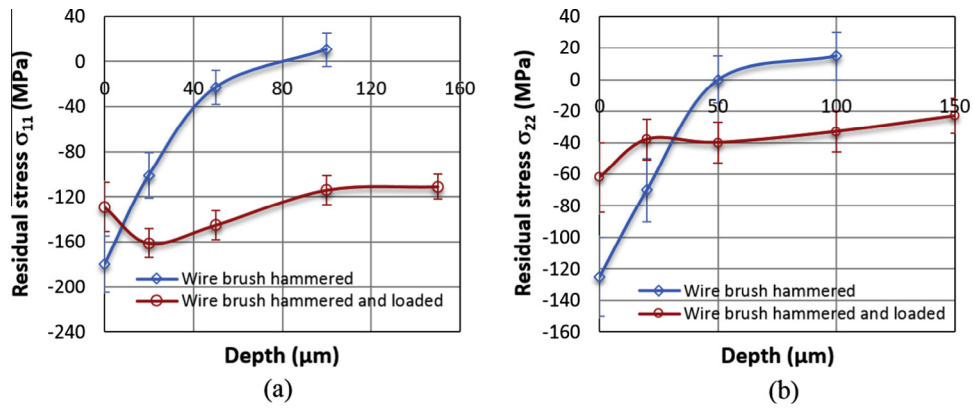
Fig. 12. Wire brush hammering residual stress redistribution under cyclic loading at $\sigma_{max} = 69.6$ MPa and $R_{0.1}$, (a) loading direction, and (b) transverse direction.
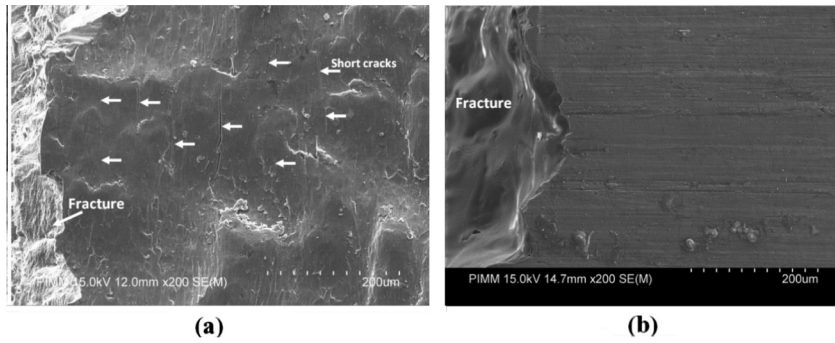
Fig. 13. Fatigue crack network-SEM examination of the notch root zone near the fracture, (a) wire brush hammered surface, and (b) machined surface.
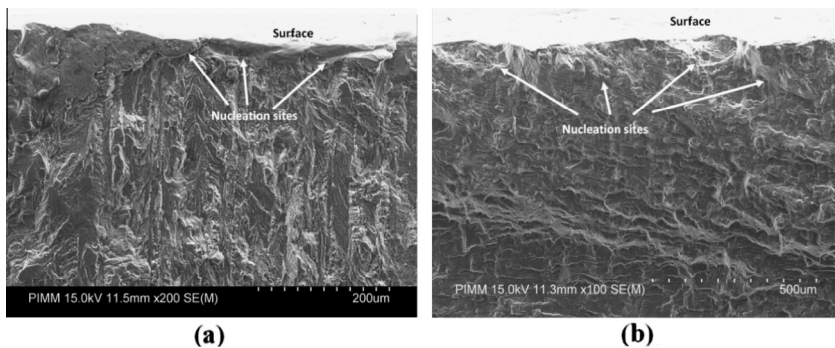
Fig. 14. Fatigue crack nucleation site, (a) surface fractured of machined specimen loaded at 64.8 MPa ($R = 0.1$) until NR = 288,282 cycles, and (b) surface fractured of wire brush hammered specimen loaded at 69.6 MPa ($R = 0.1$) until NR = 243,463 cycles.

Fig. 15. Fatigue crack growth in wire brush hammered AA 5083-H111 loaded at 69.6 MPa (R = 0.1) until NR = 243,463 cycles, (a) at 300 μm from the surface: local propagation rate = 0.5 μm/cycle, and (b) at 500 μm from the surface: local propagation rate = 1 μm/cycle.
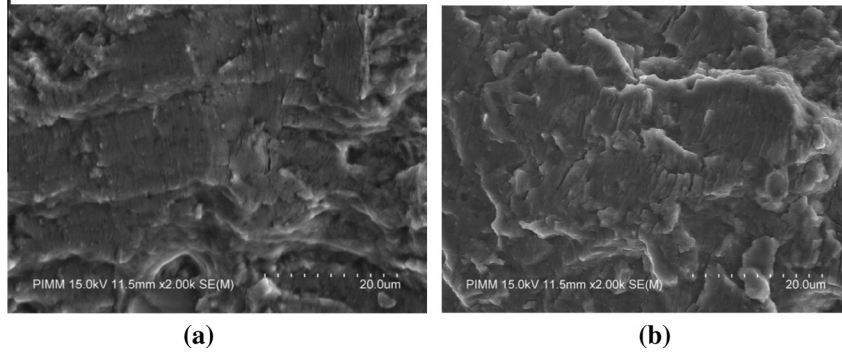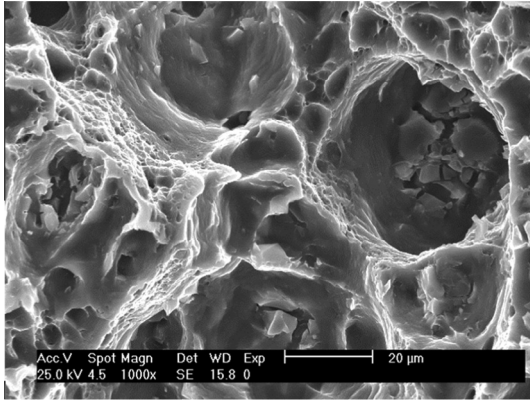

Fig. 16. Ductile final fracture of AA 5083-H111.

6.1. The Sines criterion

The Sines criterion is defined by the limitation of an equivalent stress (σ_{eq}) expressed by a linear relationship between the square root of the amplitude of J_2, denoted as $\sqrt{J_{2,a}}$, and the mean hydrostatic pressure P_m. The HCF resistance, defined for a specified number of cycles to failure (In our case 10^7 cycles), is given by the following inequality:

$$\sigma_{eq} = \sqrt{J_{2,a}} + \alpha P_m \leqslant \beta \tag{2}$$

where $\sqrt{J_{2,a}}$ and P_m are calculated from the cyclic loading tensor $\underline{\underline{\sigma}}(t)$,

$$\sqrt{J_{2,a}} = \frac{1}{2\sqrt{2}} \max_{t_i \in T} \left\{ \max_{t_j \in T} \left| \underline{S}(t_i) - \underline{S}(t_j) \right| \right\}, \tag{3}$$

$$P_m = \frac{1}{6} \left[\max_{t \in T} \left(\text{tr } \underline{\underline{\sigma}}(t) \right) + \min_{t \in T} \left(\text{tr } \underline{\underline{\sigma}}(t) \right) \right] \tag{4}$$

The material's parameters α and β of Sines criterion can be identified from two independent fatigue tests. In this work, they were determined from the four point bending tests performed at two-stress ratios $R_{0.1}$ and $R_{0.5}$.

6.2. Numerical procedure

A2D finite element model is developed for simulating the four-point bending test using ABAQUS software. The finite element model integrates meshing, loading conditions, cyclic material behavior and calculation steps.

6.2.1. Geometry and mesh

Due to symmetry only the half of the notched bending specimen is analyzed, and it is meshed using 4020 continuum-brick elements CPE4 (4-nodebilinear plan strain quadrilateral) available in ABAQUS element library. The mesh is highly refined near the notch until a length of 15 μm (Fig. 17).

6.2.2. Loading and boundary conditions

Appropriate four-point bending boundary conditions are imposed on the half of the notched bending specimen (Fig. 17). To account for the whole of specimen in calculation, an X-symmetry condition (U1 = UR2 = UR3 = 0) is applied to the cross-section of bending specimen. The bottom roller is considered as an analytical rigid part controlled by a reference point RP1, where Dirichlet boundary conditions (U1 = U2 = U3 = UR1 = UR2 = UR3 = 0) are applied. The top roller is considered as an analytical rigid part controlled by a reference point RP2 where Dirichlet boundary conditions (U1 = UR2 = 0) and force (F1 = 0, F3 = $-F(t)$) are applied to describe cyclic bending loading. The time-evolution of bending force amplitude is defined as a Fourier series:

$$F(t) = F_{max} \left[A_0 + \sum_{n=1}^{N} (A_n \cos n\omega(t - t_0) + B_n \sin n\omega(t - t_0)) \right] \tag{5}$$

where F_{max} is the maximum bending force, A_0 is the initial amplitude, A_n and B_n are constants defining the amplitude shape, $\omega = 2\pi f$ is the loading pulsation where f is the frequency and t is the loading time.

6.2.3. Material behavior law

The behavior of the aluminum alloy AA5083-H111 under cyclic loading is described in this work by the isotropic and nonlinear kinematic hardening model proposed by Lemaitre and Chaboche [37]. In this model, the yield criterion of Von Mises, the plastic flow rule and hardening variables are given by the following equations.

$$\text{Yieldcriterion } f = J_2(\sigma - X) - R - k = |\sigma - X| - R - k \leqslant 0 \tag{6}$$

$$\text{Flow rule } \dot{\varepsilon}^p = \dot{p} \frac{\partial f}{\partial \sigma} = \left(\frac{2}{3} \dot{\varepsilon}^p : \dot{\varepsilon}^p \right)^{1/2} \frac{(\sigma - X)}{|\sigma - X|} \tag{7}$$

$$\text{Isotropic hardening} \begin{cases} \dot{R} = b(Q - R)\dot{p} \\ R = Q(1 - e^{-bp}) \end{cases} \tag{8}$$

$$\text{kinematic hardening} \begin{cases} \dot{X} = \frac{2}{3} C \dot{\varepsilon}_p - \gamma X \dot{p} \\ X_M = \frac{\Delta\sigma}{2} - k = \frac{C}{\gamma} th\left(\gamma \frac{\Delta\varepsilon_p}{2} \right) \end{cases} \tag{9}$$

where X is the back stress indicating the center of the yield stress surface, R is the drag stress describing the change in the size of the yield surface, k is the initial size of the yield surface, $\dot{p}$ is the cumulated plastic strain rate.
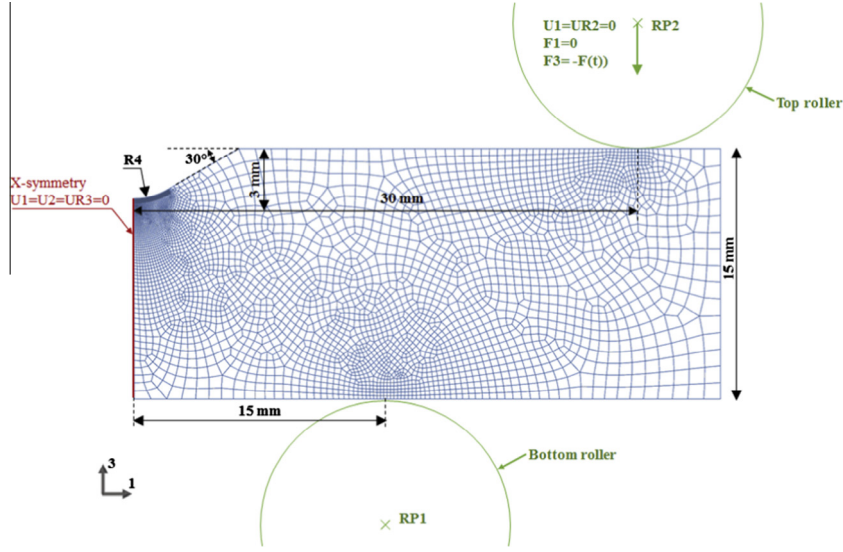
Fig. 17. Geometries, mesh and boundary conditions.

The material coefficients k, Q, b, C and γ are identified from experimental stress–strain hysteresis loops corresponding to different imposed strain range in accordance with Chaboche procedure [37]. The determined aluminum alloy AA5083-H111 coefficients are summarized in Table 9.

6.3. Accounting for initial residual stress

The experimental profiles of residual stress corresponding to both unloaded machined (Fig. 8a) and wire-brush hammered (Fig. 8b) are taken into account in the finite element model (FEM) as an initial condition using a subroutine SIGINI written in FORTRAN language. These stresses were equilibrated in a first STEP of calculation and verified with respect of experimental measurements (Fig. 18).

6.4. Accounting for initial work-hardening

The experimental profiles of machining and hammering (Fig. 7) induced work-hardening are converted to equivalent plastic strain using an empirical formula given in Eq. (10). The relationship between hardness and plastic strain is established, in this work, by hardness measurements upon incremental plastic strain resulting from tensile tests conducted on AA5083-H111 polished plate specimen in accordance to Ben Moussa method [38].

$$H_V = H_{V0} + 160\varepsilon_p^{0.62} \qquad (10)$$

The initial work-hardening converted to equivalent plastic strain profiles are taken into account in FEM as an initial condition using a subroutine HARDINI written in FORTRAN language (Fig. 19).

6.5. Stabilized stress and strain calculation

Using the numerical procedure, described below, true stress and strain fields (resulting from applied and residual stress) evolution under cyclic loading conditions were assessed for low (Fig. 20)

Table 9
Cyclic behavior law coefficients of AA 5083-H111.

E (GPa)	v	K (MPa)	Q (MPa)	b	C (MPa)	γ
70	0.33	100	103	6.44	30,000	350

and high (Fig. 21) imposed stress range. It is interesting to note that for low imposed stress range (close to fatigue limit) the stabilized state work-hardening and residual stress is reached at the first cycle due to the initial work-hardening distribution. However, for high imposed stress range, cumulated plastic strain modifies significantly work-hardening (Fig. 22a) and residual stress (Fig. 22b) distributions. Therefore, the stabilized state of residual stress (Fig. 23) and work-hardening (Fig. 24) could be assessed for various loading conditions and compared to the experimental results. An acceptable agreement between experimental and calculated profiles was observed (Figs. 23 and 24). However, due to the possible phenomenon of relaxation induced fatigue-cracks, the measured values of residual stress at near surface (lower than 20 μm) are less than the predicted value. On the other hand, the calculated plastic strain is slightly overestimated near the surface with respect to experimental assessment using microhardness measurements and converting procedure. Then, the numerical procedure is adopted as a reliable tool to identify the residual stress and work-hardening increase under cyclic loading. By means of this tool, it is demonstrated that the redistribution under cyclic loading of residual stress, as a consequence of the work-hardening change, is mostly accomplished into the first cycle for wire-brush hammered specimens as well as for machined specimens. The calculated profiles corresponding to both machined and wire-brush hammered states lead to the following comments:

- For the machined state, the effective monotonic (first cycle) loading resulting from applied and low initial compressive residual stress exceeds the tensile yield stresses of the slightly hardened layers and bulk material that promotes a plastic deformation with an extent of 1.5 and 2 mm for stress ratios $R_{0.1}$ and $R_{0.5}$ respectively. The magnitude and depth of plastic deformation depend on the applied stress level (Fig. 23a). The elastic strained under layers constrain the plastic deformed layers and generate residual stress redistribution as a result of static bending induced compressive residual stress. The magnitude and depth of the bending induced compressive residual stress with an increase in applied loading stress (Fig. 24a). The calculated stabilized surface residual stress varies from −50 MPa at stress load close to fatigue limit to −105 MPa for higher load stresses at $R_{0.1}$ and from −154 MPa at stress load close to fatigue limit to −168 MPa for higher load stresses at $R_{0.5}$ as reported in Table 10.
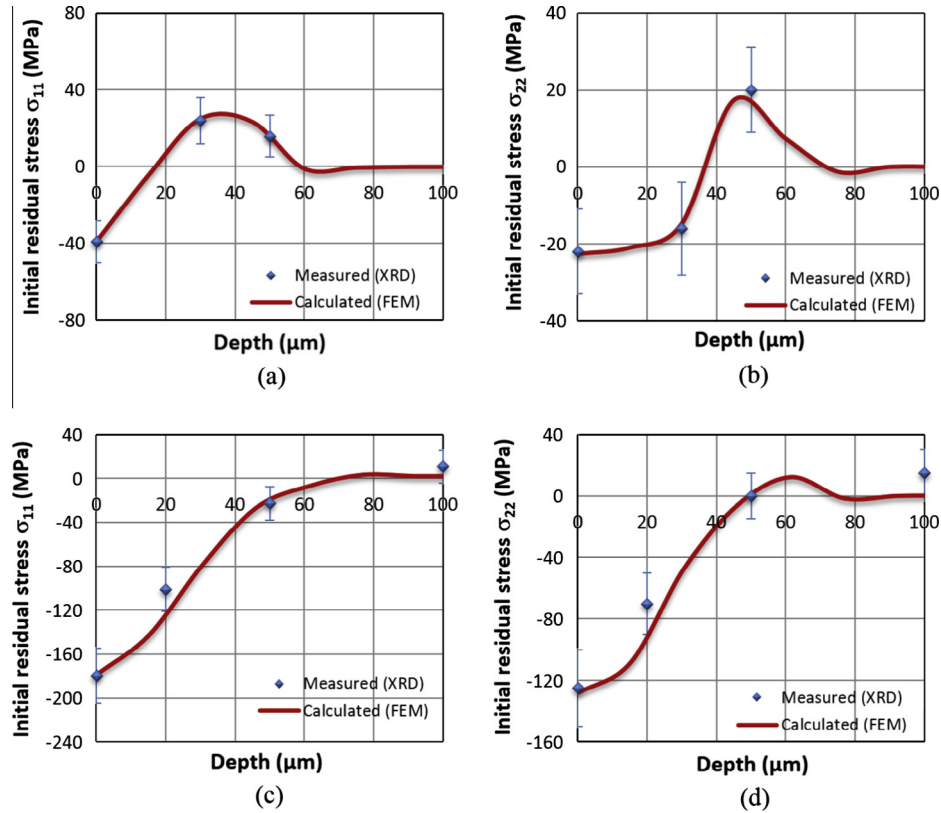
Fig. 18. Numerical accounting for original residual stress field (SIGINI-Abaqus Software) (a) machined state (loading direction), (b) machined state (transverse direction), (c) wire brush hammered state (loading direction), and (d) wire brush hammered state (transverse direction).
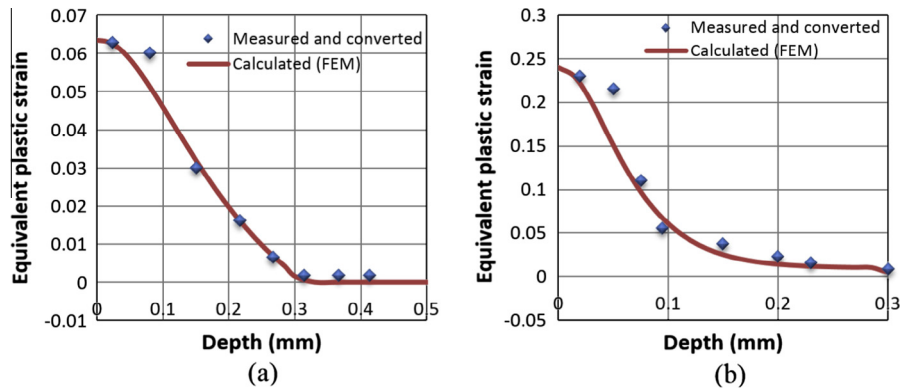

Fig. 19. Numerical accounting original work hardening distribution (HARDINI-Abaqus Software), (a) machined state, and (b) wire brush hammered state.

- For the wire-brush hammered state, the effective monotonic (first cycle) loading at stress ratio of 0.1 resulting from applied and high initial compressive residual stress, is less than the yield stress of the highly hardened layers (up to 50 µm) and exceeds the yield stress of the under layers (up to 1.5 mm) which deforms plastically (Fig. 23b). Therefore, the plastic misfit is changed and consequently the in depth residual stress redistribution is involved. The partial relaxation of the near surface residual stress is a consequence of their in-depth redistribution (Fig. 24b). The calculated stabilized surface residual stress varies from −100 MPa at stress load close to fatigue limit to −146 MPa for the lower load stresses. However, loading at stress ratio of 0.5 surpasses the tensile yield stresses of the hardened layers as well as the bulk material which promotes a plastic deformation with an extent higher than 1.2 mm

(Fig. 23b) resulting of a static bending induced compressive residual stress. The magnitude and depth of the compressive residual stress increase with increasing the applied stress level (Fig. 24b). The calculated stabilized surface residual stress varies from −160 MPa at stress load close to fatigue limit to −190 MPa for higher load stresses.

The stabilized near surface residual stress, corresponding to various experimental loading conditions, are calculated by the numerical procedure and reported in Table 10 (Column D). In addition, the peak stress and strain positions, resulting from experimental fatigue loading conditions were evaluated by numerical procedure accounting the original work-hardening and residual stress distributions, were also reported in Table 10 (Column F). These positions, considered as potential nucleation sites, comply
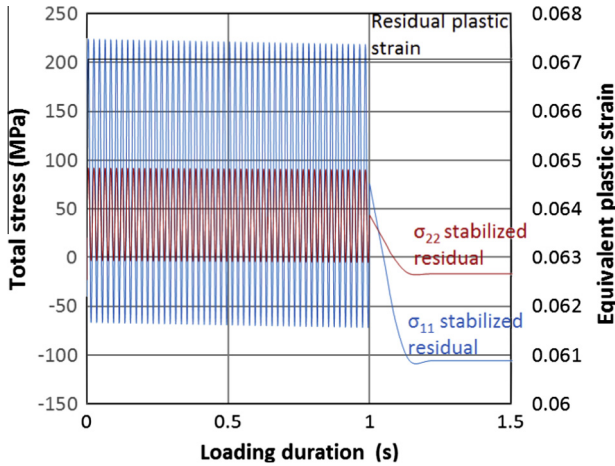
Fig. 20. Fatigue bending simulation: machined surface cyclic stress and strain evolutions at applied stress 74.4 MPa (1.3 × fatigue limit) and stress ratio $R_{0.1}$.
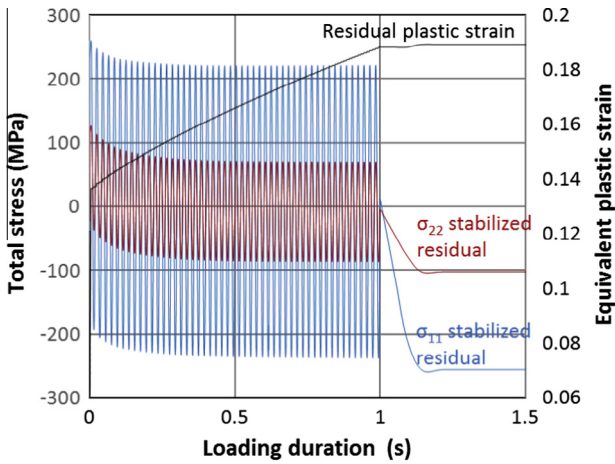

Fig. 21. Fatigue bending simulation: machined surface cyclic stress and strain evolutions at applied stress 144 MPa (2.5 × fatigue limit) and stress ratio $R_{0.1}$.

with the results of SEM examinations. They indicate that the crack nucleation sites beneath the surface are the result of the stabilized work-hardening and compressive residual stress distributions. In addition, it is observed that greater the depth of the crack source is, the greater the fatigue limit is.
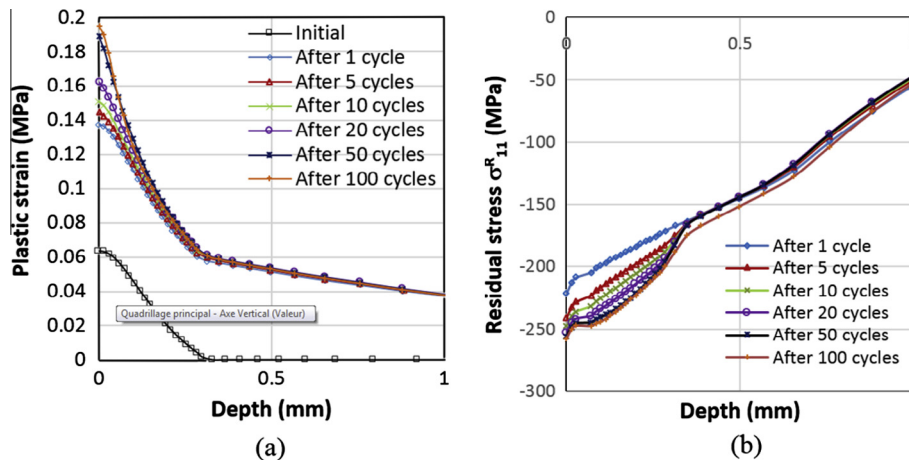
6.6. Identification and verification of the Sines criterion

Calculated stabilized stress tensors resulting from loading corresponding to experimental fatigue limits are used to identify the Sines criterion parameters reported in Table 10 (Column E), using Eq. (2). The calculated $\sqrt{J_{2,a}}$ and P_m values, derived from stabilized stress tensor corresponding to experimental fatigue test conditions, are also given in Table 10 (Column E). The predictive aptitude of the Sines criterion is verified by postponement of experimental fatigue results (fractured and unfractured) corresponding to various loading conditions (imposed nominal stress and stress ratio) for both machined and treated surfaces (Fig. 25). This figure shows that criterion line for 10^7 cycles separates fractured state (above) from unfractured ones (below) in accordance with experimental results. In addition, the effects of stress ratios $R_{0.1}$ and $R_{0.5}$, residual stress (which acts as a mean hydrostatic pressure P_m) and work-hardening (which acts on octahedral shear stress value $\sqrt{J_{2,a}}$) on fatigue limit of AA5083-H111 are observed in the Sines diagram (Fig. 25). Indeed, the improvement of fatigue strength by wire-brush hammering, as a consequence of residual stress and work-hardening, is highlighted in the Sines diagram by comparing fatigue limits of machined and hammered states at $R_{0.1}$. The Sines diagram shows that fatigue improvement is significantly reduced at $R_{0.5}$, in accordance with experimental results providing an improvement rate ranged from 5% to 20% for stress ratio $R_{0.5}$ and $R_{0.1}$, respectively.

7. Discussion

7.1. Fatigue improvement analysis

The results of the bending fatigue tests conducted in this investigation comparing the fatigue behavior of the machined and treated surfaces have demonstrated the beneficial effect of post machining treatment by wire-brush hammering on the fatigue strength of notched parts in AA5083-H111. The benefit is expressed by an increase of the fatigue limit at 10^7 cycles from 5% at stress ratio $R_{0.5}$ to 20% at stress ratio $R_{0.1}$. The potentialities of this surface treatment to enhance the fatigue resistance of aluminum alloys are promising and can be further improved by better controlling of the process parameters. However, the published data, related to the improvement rates of the fatigue strength by shot peening of aluminum alloys [5,6,11,12,20,39,40] and by wire-brush hammering of ductile austenitic stainless steels AISI 304 [31,32] fits well with the result of this study concerning AA5083-H111 as shown in Table 11. Indeed, the reported improvement rate for these materials ranged
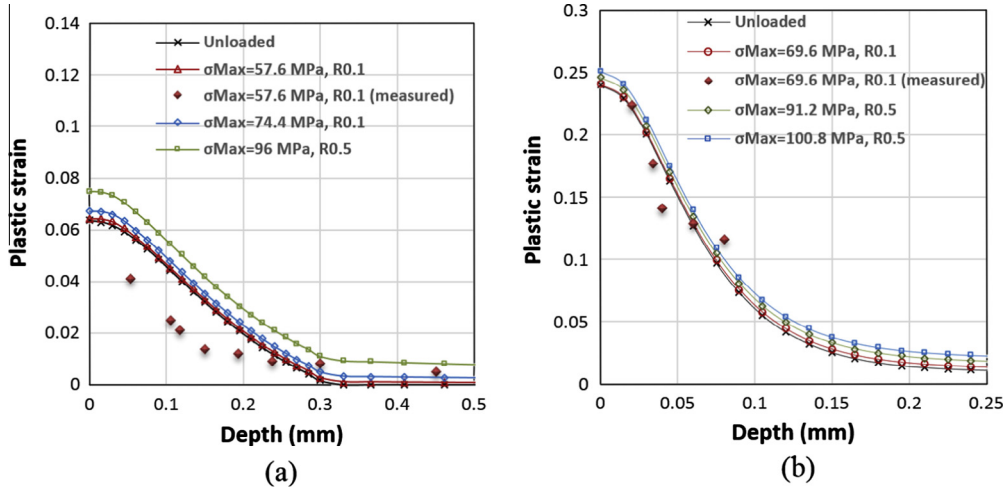

Fig. 22. Work hardening and residual stress redistribution under cyclic loading at high applied stress (σ_{max} = 144 MPa) and stress ratio $R_{0.1}$, (a) plastic strain, and (b) residual stress.

Fig. 23. Stabilized work hardening under various loading stress, (a) machined state, and (b) wire brush hammered state.
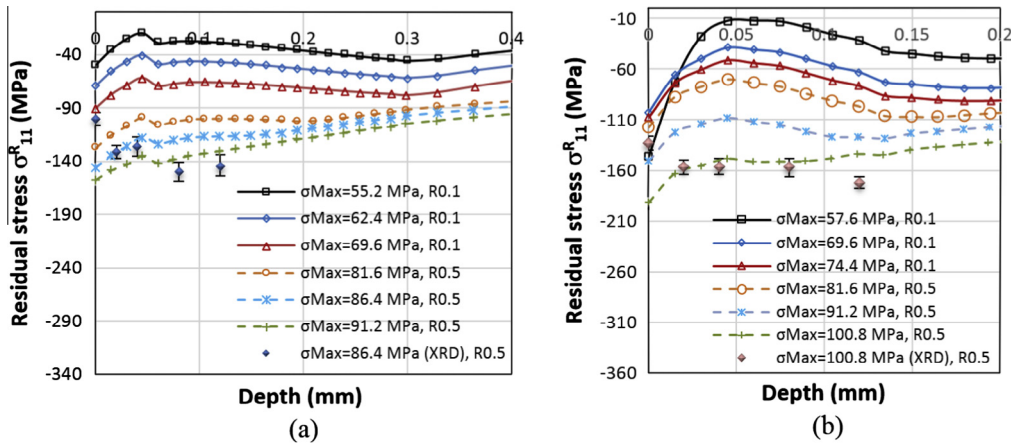

Fig. 24. Stabilized residual stress (in loading direction) under various loading paths, (a) machined state, and (b) wire brush hammered state.

from 9% [12] to 47% [6], for fatigue strength at number of cycles under than 10^7 cycles and ranged from 2.7% to 20.5% [11] for fatigue strength at 10^7 cycles depending on the material behavior, geometry of parts, loading conditions and near surface properties, which are controlled by treatment conditions. In addition, the analysis of data given in Table 11 shows that the higher the stabilized residual stress and work-hardening levels are the higher the fatigue rate improvement resulting from shot penning [6] as well as from wire-brush hammering [31] of aluminum alloys is. Besides, this treatment leads to low surface roughness (Ra $\leqslant 2$ μm), it can be considered as a substitute of shot peening for ductile materials fatigue strength improvement. It offers the lower cost, faster (few minutes) and easy implement method (commonly used for online manufacturing) for introducing compressive residual stress into the upper layers (up to -200 MPa) and high work-hardening (up to 175% of bulk material hardness) with lower surface roughness (less than 2 μm) required for fatigue aluminum alloys enhancement. Furthermore, the efficiency of wire-brush hammering as a post machining treatment of notched parts has been demonstrated in this study. Whereas, shot peening is frequently applied to the external surfaces of mechanical components.

7.2. Effect of the stabilized surface characteristics on the fatigue-crack nucleation and growth

The fatigue resistance improvement can be explained by the enhancement of the wire-brush hammered surface integrity with

respect to the machined one. The experimental and numerical results of this study showed that the beneficial effect of the wire-brush is a result of coupling of surface morphology, near surface stabilized work-hardening and residual stress field. The relative beneficial contributions of each factor are discussed on the basis of its effect on fatigue-crack nucleation and growth.

7.2.1. Effect of surface morphology and roughness

It has been shown that the wire-brush hammering removes the groves and surface flaw, generated by the previous machining operation (Fig. 5), which are expected to act as micro-notches, promoting fatigue-crack nucleation, as reported by previous works [21,30,34]. The detrimental effect of surface roughness on the fatigue strength is quantified by Benedetti et al. [6] through fatigue tests conducted on the shot peened AA7075-T651 as given in Table 11. Authors show a decrease of an improvement rate of the fatigue limit at 5×10^6 cycles from 47% to 13% at R_{-1} and from 23% to 21% at R_0 with an increasing of surface roughness (Ra) from 1.35 μm to 3.39 μm. This detrimental effect of surface texture is reduced or avoided by the wire-brush hammering of AA5083-H111 machined surfaces, which generates topographical features with low stress factor concentration comparatively to machining groves and shot peening surface dimples (Fig 5a and b). Indeed, the selected conditions of AA5083-H111 wire-brush hammering slightly improves the surface roughness (Ra = 1.8 μm) with respect to the prior machined surface (Ra = 2.4 μm) and much more compared to less intense shot peened condition (Ra = 9 μm). This

Table 10
Effect of stabilized work hardening and residual stress on AA 5083-H111 fatigue life (experimental and numerical results).

| A	B		C	D			E				F	
Surface preparation mode	Loading conditions		Fatigue test results				Sines criterion				Crack nucleation site	
	Stress ratio	Maximal notch root stress (MPa)	Fatigue life N (cycles)	σ_{11}^{RS} (MPa)	σ_{22}^{RS} (MPa)	ε_p (%)	P_m (MPa)	$\sqrt{J_{2,a}}$ (MPa)	β (MPa)	α	Calculated crack initiation point (μm)	Experimented crack initiation point (μm)
Machined	$R_{0.1}$	55.2	10^7 (NF)	−50	−18	6.43	29	55	65	0.26	0–30	
		57	**Fatigue limit at 10^7 (NF) cycles**	**−54**	**−18**	**6.45**	**29**	**58**				
		60	10^7 (NF) / 10^7 (NF) / 352,891 / 465,684	−62	−17	6.48	30	60				
		62.4	862,317 / 581,391 / 2,821,131 / 10^7 (NF)	−70	−17	6.51	30	62				
		64.8	10^7 (NF) / 10^7 (NF) / 288,282 / 887,049	−77	−16	6.54	30	65				20–50 (Fig. 14a)
		67.2	333,575 / 392,840 / 10^7 (NF)	−84	−16	6.58	31	67				
		69.6	388,102	−90	−16	6.61	31	70				
		72	1,259,875	−97	−16	6.66	31	72				
		74.4	186,522 / 684,120	−105	−16	6.7	32	75				
	$R_{0.5}$	81.6	10^7 (NF)	−127	−17	6.88	66	45				
		86.4	10^7 (NF) / 10^7 (NF) / 10^7 (NF)	−146	−20	7.03	68	46.4				
		89	**Fatigue limit at 10^7 cycles**	**−154**	**−23**	**7.14**	**69**	**48**				
		91.2	1,052,227 / 834,005 / 630,230	−158	−26	7.24	70	49				
		96	302,688	−168	−32	7.49	71	51				
Wire brush hammered 100–300	$R_{0.1}$	57.6	10^7 (NF)	−146	−111	24.01	−34	58				
		60	10^7 (NF)	−135	−107	24.01	−28	60				
		62.4	10^7 (NF)	−119	−105	24	−23	62				
		64.8	10^7 (NF)	−102	−103	23.99	−19	65				
		67.2	10^7 (NF) / 10^7 (NF)	−101	−96	24.02	−15	67				
		68.4	**Fatigue limit at 10^7 cycles**	**−102**	**−92**	**24.03**	**−13**	**68**				
		69.6	243,463 / 451,491	−102	−89	24.05	−11	70				70 to 150 (Fig. 14b)
		72	408,877	−105	−82	24.08	−8	72				
		74.4	115,498	−107	−75	24.12	−5	74			90–200	
	$R_{0.5}$	81.6	10^7 (NF)	−117	−55	24.27	36	44			70–160	
		86.4	10^7 (NF)	−133	−46	24.4	43	46				
		91.2	10^7 (NF) / 920,946 / 730,435	−151	−40	24.6	49	49				
		93.6	**Fatigue limit at 10^7 cycles**	**−163**	**−39**	**24.72**	**52**	**50**				
		96	386,257 / 426,599	−171	−39	24.8	54	51				
		100.8	362,316	−192	−39	25.1	59	54			30–100	

The bold values are significant because they are used to plot the Sines criterion line separating fractured states to unfractured ones (Fig. 25).

enhanced surface quality, added to the compressive residual stress field, promotes the nucleation of short (Fig. 13a) rather than long (Fig. 13b) fatigue-cracks. This found is supported by Koster [41] who concludes that fatigue life primarily depends on workpiece residual stress and surface microstructure, rather than roughness ranged from 2.5 μm to 5 μm Ra. In contrast, surface roughness in excess of 0.1 μm Ra could have a strong influence on the fatigue life in the absence of residual stress.

7.2.2. Effect of stabilized work-hardening

It has been established that the work-hardening characterized by the height and width of the hardness profile changes significantly under cyclic loading as illustrated in Fig. 10. This modification depends on the work-hardening and level of effective stress gradient (applied and residual stresses). The experimental profiles show a deeper work-hardening of loaded wire-brush hammered specimen (Fig. 10b) compared with the machined one (Fig. 10a).
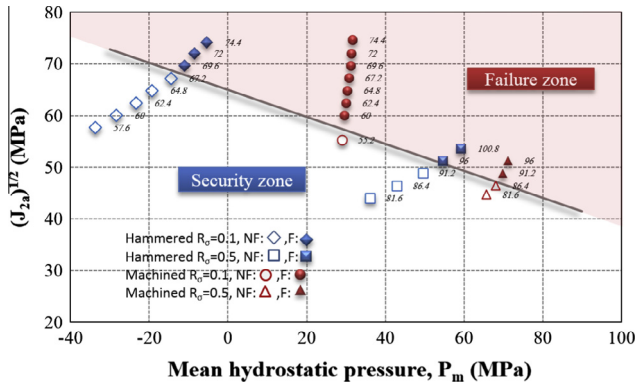
Fig. 25. Sines diagram with criterion accounting for work hardening and residual stress.

The numerical procedure attributes this significant evolution to the plastic strain increment accomplished during the first loading cycle (Fig. 20) which causes the residual stress redistribution (Figs. 23 and 24), and consequently moving of peak stress and strain as reported in Table 10 (Column F). Indeed, the fatigue-cracks in wire-brush hammered specimens often nucleate in subsurface (70–150 μm) due to peak tensile stress resulting from summation of applied tensile and compressive residual stresses (Fig. 14b). However, the sources of fatigue-crack nucleation in machined specimen is very close to the surface (0–30 μm), which contribute to the loss of the crack initiation lifetime (Fig. 14a). In addition, the analysis of data given in Table 11 shows that the higher fatigue improvement rates attained by shot peening [6] and by wire brush hammering [31] are obtained for higher work hardening rate. On the other hand, the strain-hardened layers promotes rapid propagation and therefore causes lower crack growth resistance as highlighted by SEM micro-fractographs showing cleavage and crystallographic aspects of hardened layer fracture (Fig. 14). The rapid propagation of fatigue-cracks during the earlier stages of mechanically treated surfaces is often attributed, by several

authors [22–24,30,31,34], to the work-hardened material embrittlement.

7.2.3. Effect of stabilized residual stress

Since the residual stresses is expected to be responsible for a larger contribution of wire-brush hammering to enhance fatigue performance of AA5083-H111 notched specimens, it is of paramount importance to evaluate their stability under cyclic loading in order to discuss of their effect on the fatigue-crack nucleation and growth. It should be noted that XRD measurements showed a partial relaxation of hammering induced near surface compressive residual stresses (Fig. 12) and an additional compressive residual stress induced by cyclic loading of machined specimen (Fig. 11). This tendency was proved by numerical simulation that showed that the most changes in the residual stress profile occurred on the first cycle as consequences of work-hardening redistribution (Fig. 20). In addition, it has been established that the magnitude and depth of compressive residual stress depend on more applied stress rather than number of cycles (Fig. 24). The same residual stress relaxation tendency depending on the applied stress was observed for the case of AISI 304 treated by wire brush hammering [42]. Therefore, the calculated near surface residual stress reported in Table 10 (Column D) could be used to explain the wire-brush hammering fatigue improvement. Indeed, for an applied stress level close to fatigue limit at stress ratio of 0.1, the stabilized compressive residual stress in loading direction reaches -102 MPa at the surface of hammered specimen against -54 MPa at the surface of machined specimen. At stress ratio of 0.5, stabilized residual stresses are -163 MPa and -154 MPa for hammered and machined specimens, respectively. On the basis of well-established beneficial effect of compressive residual stress in fatigue enhancement [3,30,34,42], the experimental assessed improvement rates of fatigue limit equal to 20% and 5% at stress ratio 0.1 and 0.5 respectively are expected. The Sines criteria accounting this effect predicts with a good accuracy (the uncertainty is lower than 3%) these improvement rates (Fig. 25). This result is also supported by the experimental analysis of surface

Table 11
Fatigue strength improvement by shot peening and wire brush hammering.

Surface treatment conditions		Material	Surface characteristics						Fatigue conditions and results					Refs.
			Roughness		Hardening	Residual stress			Loading conditions			Results		
						Initial		Stabilized						
Treatment	Almen intensity		Surface roughness		Work hardening rate $\frac{\Delta H_V}{H_{V0}}$	σ_0^R (MPa)	Depth (mm)	σ_s^R (MPa)	Specimen geometry	Stress ratio R	Fatigue life N (cycles)	Fatigue limit σ_D (MPa)	Fatigue improvement rate (%)	
			Ra (μm)	Rt (μm)										
Shot peening	0.2A	2024 T3	4.1			-180	0.5		Notched	-1	10^7	250	**25**	[20]
		2024 T6				-325	0.44					225	**12.5**	
		2024 T351	4.3	25	0.27	-165	0.2	-90	Not notched	0.1	7.10^6	270	**26**	[39]
			4.5	30										
		6082 T5	1.7		0.45	-135	0.25			0.1		98	**40**	[40]
	4.5 N	7075 T651	1.35	6.1	1.07	-285	0.075	-270	Not notched	-1	5.10^6	213	**47**	[6]
										0		156	**23**	
	4.5A		3.39	15.2	1.02	-344	0.3	-330	Not notched	-1	5.10^6	164	**13**	[5]
										0		154	**21**	
	0.1A	7050 **T7451**	1.29	6.12		-175	0.15		Not notched	-1	10^7	190	**2.7**	[11]
	0.2A		4.15	16.5		-370	0.27					223	**20.5**	
	9.6 (SP170)		3.929			-473	0.25		Not notched	0.1	10^5	262	**30**	[12]
											10^6		**9**	
Double shot peening	4.5A and 4.5 N	7075 T651	3.41	16.4	1.01	-366	0.3	-340	Not notched	-1	5.10^6	189	**30**	[6]
										0	2.10^6	176	**38.6**	[5]
	0.2A + 0.1A	7050 T7451	2.06	7.46		-370	0.25		Not notched	-1	10^7	250	**35**	[11]
Wire brush hammering		AISI 304	2.2	10.2	1.4	-220	0.7		Notched	0.1	2.10^6	285	**26**	[31]
	5.9 N	5083 H111	1.8	12.5	0.75	-180	0.08		Notched	0.1	10^7	114	**20**	This study
										0.5		156	**5**	

Bold values denote the fatigue improvement rate, where its maximization is the main aim of the paper.

fracture which showed transfer of the crack sources beneath the surface (at 100–200 μm from the surface) by the wire-brush hammering of AA5083-H111 (Fig. 14). Then, their appearance at the hammered surface, in the form of short cracks, is likely caused by brittle fracture of work-hardened upper layers (Fig. 13a). Their stability against coalescence is promoted by the compressive residual stress field, which is considered as the main source of the crack closure. Indeed, the crack grow at a highly reduced rate, less than 0.5 μm/cycle into compressive residual stress field and at a double growth rate (1 μm/cycle) outside (Fig. 15).

8. Conclusions

It has been established that the bending fatigue limit at $R_{0.1}$ for 10^7 cycles is 20% increased by the wire-brush hammering used as a post machining treatment of AA5083-H111 notched specimens. The wire-brush hammering of notched samples increases the total fatigue life, even when operating in LCF conditions. The notch shape does not affect the efficiency of the treatment. The improvement is mainly the result of stabilized compressive residual stress and work-hardening profiles making the fatigue-crack nucleation source beneath the surface and their propagation rate at reduced level. The importance of surface topography, stabilized work-hardening and residual stress on the resistance of fatigue-crack nucleation and growth has been highlighted and experimental results were compared with numerical results relating to fatigue strength. The numerical approach was set up to predict work-hardening and residual stress evolution for various cyclic loading paths. It can also predict the preferential crack initiation sites that are located close to the surface for machined state and below the surface for wire-brush hammered state. The fatigue resistance of AA5083-H111 notched specimens has been satisfactorily predicted by a multiaxial fatigue criterion accounting the effect of both residual stresses and work-hardening.

References

[1] Fathallah R, Laamouri A, Sidhom H, Braham C. High cycle fatigue behavior prediction of shot-peened parts. Int J Fatigue 2004;26:1053–67.
[2] Fathallah R, Sidhom H, Braham C, Castex L. Effect of surface properties on high cycle fatigue behaviour of shot peened ductile steel. Mater Sci Technol 2003;19:1050–6.
[3] Sidhom N, Laamouri A, Fathallah R, Braham C, Lieurade HP. Fatigue strength improvement of 5083 H11 Al-alloy T-welded joints by shot peening: experimental characterization and predictive approach. Int J Fatigue 2005;27:729–45.
[4] Sidhom N, Braham C, Lieurade HP. Fatigue life evaluation of shot peened al-alloys 5083 H11 T-welded joints by experimental and numerical approaches. Welding World 2007;51:50–7.
[5] Benedetti M, Fontanari V, Monelli BD. Plain fatigue resistance of shot peened high strength aluminium alloys: effect of loading ratio. Procedia Eng 2010;2:397–406.
[6] Benedetti M, Fontanari V, Scardi P, Ricardo CLA, Bandini M. Reverse bending fatigue of shot peened 7075–T651 aluminium alloy: the role of residual stress relaxation. Int J Fatigue 2009;31:1225–36.
[7] Kopsov IE. The influence of hammer peening on fatigue in high-strength steel. Int J Fatigue 1991;13:479–82.
[8] Liu J, Gou WX, Liu W, Yue ZF. Effect of hammer peening on fatigue life of aluminum alloy 2A12-T4. Mater Des 2009;30:1944–9.
[9] Mhaede M. Influence of surface treatments on surface layer properties, fatigue and corrosion fatigue performance of AA7075 T73. Mater Des 2012;41:61–6.
[10] Juijerm P, Altenberger I, Scholtes B. Fatigue and residual stress relaxation of deep rolled differently aged aluminium alloy AA6110. Mater Sci Eng, A 2006;426:4–10.
[11] Gao YK. Improvement of fatigue property in 7050–T7451 aluminum alloy by laser peening and shot peening. Mater Sci Eng, A 2011;528:3823–8.
[12] Luong H, Hill MR. The effects of laser peening and shot peening on high cycle fatigue in 7050–T7451 aluminum alloy. Mater Sci Eng, A 2010;527:699–707.
[13] Cherif A, Pyoun Y, Scholtes B. Effects of ultrasonic nanocrystal surface modification (UNSM) on residual stress state and fatigue strength of AISI 304. J Mater Eng Perform 2010;19:282–6.
[14] Gao Y-k, Lu F, Wang Q. Influence of pulsed electron beam polishing modification on surface morphologies of TC21 titanium alloy. Heat Treat Met 2009;34:42–4.
[15] Tange A, Ando K. Improvement of spring fatigue strength by new warm stress double shot peening process. Mater Sci Technol 2002;18:642–8.
[16] Terres MA, Laalai N, Sidhom H. Effect of nitriding and shot-peening on the fatigue behavior of 42CrMo4 steel: experimental analysis and predictive approach. Mater Des 2012;35:741–8.
[17] Tsuji N, Tanaka S, Takasugi T. Evaluation of surface-modified Ti–6Al–4V alloy by combination of plasma-carburizing and deep-rolling. Mater Sci Eng, A 2008;488:139–45.
[18] Tian Y, Shin YC. Laser-assisted burnishing of metals. Int J Mach Tools Manuf 2007;47:14–22.
[19] Zhu Y-L, Wang K, Li L, Huang Y-L. Evaluation of an ultrasound-aided deep rolling process for anti-fatigue applications. J Materi Eng Perform 2009;18:1036–40.
[20] Wagner L. Mechanical surface treatments on titanium, aluminum and magnesium alloys. Mater Sci Eng, A 1999;263:210–6.
[21] Novovic D, Dewes RC, Aspinwall DK, Voice W, Bowen P. The effect of machined topography and integrity on fatigue life. Int J Mach Tools Manuf 2004;44:125–34.
[22] Wagner L, Lütjering G. Influence of shot peening parameters on the surface layer properties and the fatigue life of Ti–6Al–4V. In: Fuchs HOe, editor. Proceedings of 2nd international conference shot peening. Paramus (NJ): American Shot Peening Society; 1984. p. 194–200.
[23] Wagner L. Surface Performance of Titanium Alloys, TMS, City 1997.
[24] de los Rios ER, Walley A, Milan MT, Hammersley G. Fatigue crack initiation and propagation on shot-peened surfaces in A316 stainless steel. Int J Fatigue 1995;17:493–9.
[25] Ochi Y, Masaki K, Matsumura T, Sekino T. Effect of shot-peening treatment on high cycle fatigue property of ductile cast iron. Int J Fatigue 2001;23:441–8.
[26] Wang S, Li Y, Yao M, Wang R. Fatigue limits of shot-peened metals. J Mater Process Technol 1998;73:57–63.
[27] Sharp P, Clayton J, Clark G. The fatigue resistance of peened 7050–T7451 aluminium alloy—repair and re-treatment of a component surface. Fatigue Fract Eng Mater Struct 1994;17:243–52.
[28] Luo W, Noble B, Waterhouse RB. The effect of shot-peening intensity on the fatigue and fretting-fatigue behaviour of an aluminium alloy. In: Niku-Lari A, editor. Advances in Surface Treatments. Pergamon; 1987. p. 145–53.
[29] Ghanem F, Fredj NB, Sidhom H, Braham C. Effects of finishing processes on the fatigue life improvements of electro-machined surfaces of tool steel. Int J Adv Manuf Technol 2011;52:583–95.
[30] Makhlouf K, Sidhom N, Khlifi A, Sidhom H, Braham C. Low cycle fatigue life improvement of AISI 304 by initial and intermittent wire brush hammering. Mater Des 2013;52:1088–98.
[31] Ben Fredj N, Ben Nasr M, Ben Rhouma A, Sidhom H, Braham C. Fatigue life improvements of the AISI 304 stainless steel ground surfaces by wire brushing. J Mater Eng Perform 2004;13:564–74.
[32] Ben Fredj N, Sidhom H, Braham C. Effect of the cryogenic wire brushing on the surface integrity and the fatigue life improvement of the AISI 304 stainless steel ground components. Fract Nano Eng Mater Struct 2006:1303–4.
[33] Normalization Francaise A 03-405: Essais de Fatigue, Tour Europe. Paris La Defense: Lassociation Francaise de Normalisation. L'assotiation Francaise de Normalisation; 1991.
[34] Sidhom N, Makhlouf K, Khlifi A, Sidhom H, Braham C. Low cycle fatigue life improvement of AISI316 by wire brush hammering; 2014.
[35] Sidhom N, Sidhom H, Braham C, Lédion J. Effects of brushing and shot-peening residual stresses on the fatigue resistance of machined metal surfaces: experimental and predicting approaches. Materials science forum. Trans Tech Publ; 2011. p. 290–5.
[36] Sines G. Behaviour of metals under complex static and alternating stresses. New York: Mcgraw-Hill; 1959.
[37] Lemaitre J, Chaboche J. Mécanique des matériaux solides. Paris: Dunod; 2001.
[38] Ben Moussa N, Sidhom H, Braham C. Numerical and experimental analysis of residual stress and plastic strain distributions in machined stainless steel. Int J Mech Sci 2012;64:82–93.
[39] Asquith DT, Yerokhin AL, Yates JR, Matthews A. Effect of combined shot-peening and PEO treatment on fatigue life of 2024 Al alloy. Thin Solid Films 2006;515:1187–91.
[40] Benedetti M, Bortolamedi T, Fontanari V, Frendo F. Bending fatigue behaviour of differently shot peened Al 6082 T5 alloy. Int J Fatigue 2004;26:889–97.
[41] Koster W. Effect of Residual Stress on Fatigue of Structural Alloys. In: International A, editor. In: Proceedings of the Third International Conference. Indianapolis, Indiana, USA; 1991. p. 1–9.
[42] Laamouri A, Sidhom H, Braham C. Evaluation of residual stress relaxation and its effect on fatigue strength of AISI 316L stainless steel ground surfaces: experimental and numerical approaches. Int J Fatigue 2013;48:109–21.